# Au core stabilizes CO adsorption onto Pd leading to $CO_2$ production

E.H. Fontes [a, *], J. Nandenha [a], R.F.B. De Souza [a], F.C.T. Antonio [b], P. Homem-de-Mello [b], A.O. Neto [a]

[a] Instituto de Pesquisas Energéticas e Nucleares, IPEN/CNEN-SP, Av. Prof. Lineu Prestes, 2242 Cidade Universitária, CEP 05508-900, São Paulo, SP, Brazil
[b] Centro de Ciências Naturais e Humanas, Universidade Federal Do ABC, Av. Dos Estados, 5001, Bairro Santa Terezinha, Santo André, SP, Brazil

## ARTICLE INFO

## ABSTRACT

Au core and Pd shell supported on carbon structure Au@Pd/C can cleave the C−C bond of ethanol molecules leading to the production of a relatively high amount of $CO_2$ when compared with Pd/C electrocatalyst as the attenuated total reflectance - Fourier transform infrared (ATR-FTIR) experiment shows. Density functional theory (DFT) calculations showed that this could be explained by the oxidation of CO species adsorbed into Pd sites that has a modified electronic structure compared with Pd/C. In terms of DFT analysis, the highest thermodynamical stability of CO in Pd shell with Au core atoms, when compared with Pd/C is because of the increase of virtual orbital states near Fermi level that can be occupied by valence electrons of CO molecule. The d-band center shift is experimentally verified using the valence band X-ray photoelectron spectroscopy and theoretically predicted by the Generalized Koopmans' Theorem. Besides that, Au@Pd/C electrocatalyst has a better electrochemical activity when compared with Pd/C.

© 2020 The Author(s). Published by Elsevier Ltd. This is an open access article under the CC BY-NC-ND license (http://creativecommons.org/licenses/by-nc-nd/4.0/).

## 1. Introduction

One of the limiting steps concerning ethanol oxidation reaction (EOR) is the difficulty of achieving its complete oxidation. The design of electrocatalysts able to cleave the C−C bond of ethanol molecules is nowadays one of the indispensable research field [1−4] Furthermore, the slow reaction kinetics and the poisoning effect caused by the presence of the adsorbed species, such as acetate and carbonate ions, are also issues that need to be overcome [3,5−8]. The investigation of new electrocatalysts able to oxidize intermediate adsorbed species is imperative not only in electrochemical systems, which has ethanol as a protagonist but rather other types of alcohols, for instance, methanol [9] and glycerol [10].

Core-shell nanoparticles, for instance, Au seeds and Pd shell, are well known to have poisoning tolerance and, consequently, high activity regarding EOR [3,4,11,12]. The synergistic effect between Au and Pd atoms seems to improve the EOR. Besides that, alkaline media has some advantages over acid media concerning EOR, for instance, reduced cost concerning electrocatalysts manufacturing and also increases the efficiency by improving the reaction kinetics [13−15]. Au-based catalysts are also known to have great alcohol

oxidation performance in alkaline medium because of its higher tolerance against the formation of poisoning surface oxides [16].

The synergistic effect abovementioned is often attributed to the lattice constraint induced by Au core atoms in Pd layer, and this effect is known as the pseudomorphic layer model [17]. This effect is also associated with the Pd d-band center shift as well as an increase in the density of states (DOSs) near the Fermi level [17,18]. In fact, Hsu et al. [18] point out that the actual connection between catalytic activity and electronic structure is better correlated trough analyzing the DOS near the Femi level. Some authors investigated the DOS of such materials pursuing to make correlations between catalytic activity and electronic structure [17,19]. Nevertheless, the explanation of why some properties are desirable is still not clear. Gorzkowski and Lewera [17] stress out the need to measure the electronic structure to better understand the factors responsible for the changes in catalytic activity, and Pereira and Miranda [19] intend to verify if the d-band center theory [20,21] was consistent with their results. But still, they were not interested in actually calculate the DOS and local DOS (L-DOS) of their materials.

Most of the density functional theory (DFT) calculations focused on investigating the EOR pathways on metal surfaces [19,22]. Our aim in this work is to examine the influence of Au atoms in Pd anchored on carbon structure (Pd7/C), leading to a bimetallic material (Au5@Pd2/C) via DFT and using experimental techniques (Pd/

* Corresponding author.
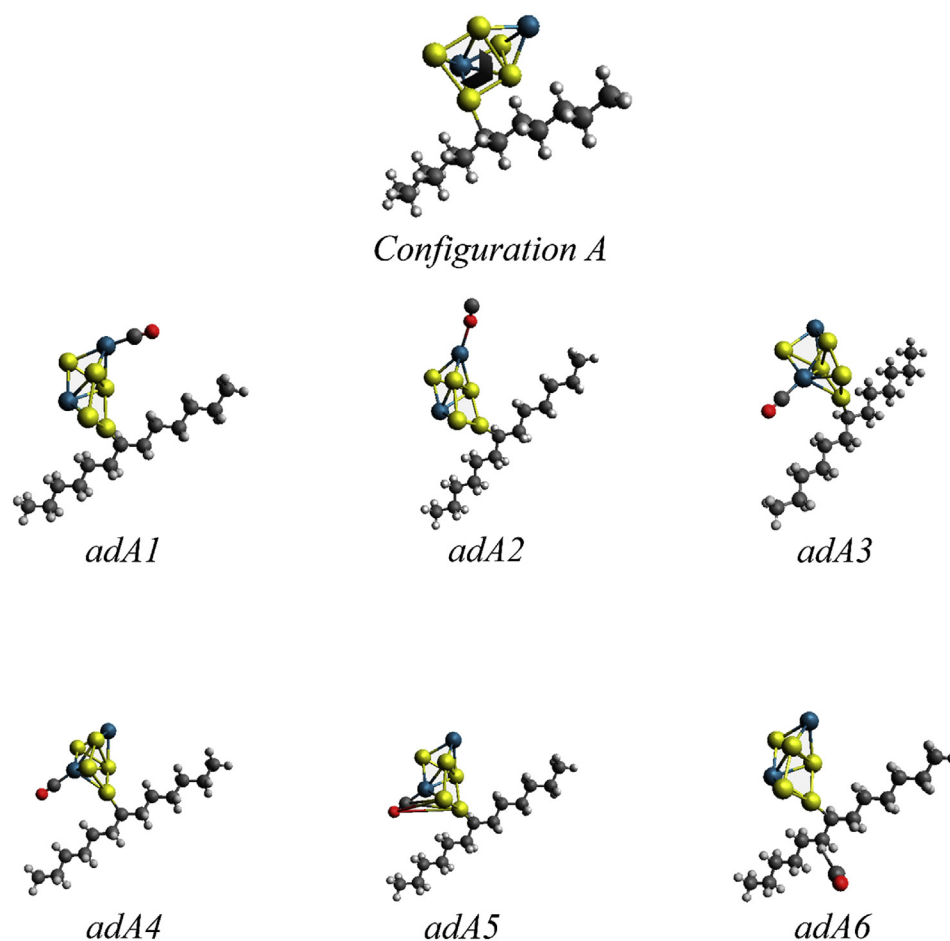E-mail address: ericfisico@usp.br (E.H. Fontes).

**Fig. 1.** Obtained geometry for configuration A [Au5@Pd2/C]A and CO adsorption geometries. Yellow balls are Au atoms, blue ones are Pd atoms, red ones are oxygen atoms, dark gray ones are carbon atoms, and white balls are hydrogen atoms. (For interpretation of the references to color in this figure legend, the reader is referred to the Web version of this article.)

C and Au@Pd/C). Furthermore, we intend to analyze through DFT the thermodynamical stability of CO molecule on Pd7/C and Au5@Pd2/C materials, because this can explain if the oxidation of CO molecules to $CO_2$ is possible to occur in core-shell nanoparticles Au@Pd/C surfaces.

## 2. Methods

### 2.1. Au@Pd/C and Pd/C synthesis and characterization

Au@Pd/C was synthesized by direct growth of Pd shell on the surface of Au seeds. The preparation follows [27]. It was used 0.1 mmol of $HAuCl_4 \cdot 3H_2O$ dissolved in 10 mL of oleylamine placed in three-necked flask equipped with a condenser and a stir bar. The solution was heated to 150°C and kept for 1 h until the $Au^{3+}$ ions was reduced by the reducing and capping agent oleylamine. After this, 0.015 mmol of Pd (acetylacetonate)$_2$ was swiftly added to the Au seeds + oleylamine solution under vigorous stirring at 150°C for more 2 h. After this, the nanoparticles were purified by precipitation with methanol, re-dispersed in 10 mL of toluene, and then added to the carbon Vulcan XC72 support. Palladium (II) acetylacetonate (Pd (acac)2, 99%), gold (III) chloride trihydrate ($HAuCl_4 \cdot 3H2O$, ACS reagent, $\geq$ 49.0% Au basis), oleylamine (70%, technical grade), and Nafion® 117 solution (5% in a mixture of lower aliphatic alcohols and water) were purchased from Sigma-Aldrich.

Pd/C was prepared by the borohydride reduction method [28]. The reducing agent sodium borohydride (Sigma Aldrich) was dissolved in 0.01 mol $L^{-1}$ solution of NaOH. The $Pd(NO_3)_2 \cdot 2H_2O$ metal salt was added in a mixture of water/2-propanol (50/50, v/v) along with Carbon Vulcan XC72 (Cabot). The mixture was taken to an ultrasonic homogenizer for 10 min, and then the reducing agent was added swiftly under stirring at room temperature acting for 1 h. Immediately after this, the mixture was filtered and washed with (Milli-Q water) and then dried at 70°C for 2 h [29].

Valence band X-ray photoelectron spectroscopy was made using the K-alpha (Thermo Scientific) spectrometer at LNNANO/CNPEM facility. The X-ray spot size was set to 400 $\mu m$, and the binding energy range was set to −10 to 10 eV.

Images and micrographs were obtained by the TEM-FEG JEM 2100F microscope equipped with a scanning image observation device. These analyses were also performed at LNNANO/CNPEM facilities. The electron gun used is the ZrO/W (100) Schottky field emission electron source with an accelerating voltage of 200 kV, and the CCD camera is the Gatan 2k x 2k.

Cyclic voltammetry (CV) and chronoamperometry experiments were carried out using the potentiostat PGSTAT30 AutoLab. The technique used to prepare the working electrodes was the ultrathin porous coating [29], with Ag/AgCl (3 M of KCl) reference electrode and Pt counter electrode. The electrochemical and spectroelectrochemical experiments were made in a concentration of 0.5 mol $L^{-1}$ of KOH +75 mmol $L^{-1}$ of EtOH as follows [30].

*In situ* ATR-FTIR (potential applied vs. absorption spectra) measurements were made using the Nicolet 6700 FTIR spectrometer equipped with an MCT detector. The electrochemical cell was made with a Teflon cell, and the ATR accessory is the Miracle Pike (which internal reflection element is ZnSe). The working electrodes and the operational parameters concerning the electrochemical cell are the same as the electrochemical measurements. The FTIR parameters can be found in study by Fontes et al. [28], and background collection was performed at −0.85 V. The electrolyte solution used was 0.5 mol L$^{-1}$ of KOH.

## 2.2. DFT calculations

The design of the proposed electrode is quite difficult because this is inhomogeneous. So, we employed strategies developed before [23,24,26,43] and proposed cluster structures to evaluate the effect of each component: seven metallic atoms (Au and Pd) [24] and carbon support (14 carbon atoms saturated by hydrogen atoms) [24,26,43]. CO adsorption energy was calculated as [24]:

E(CO on Pd7/C or Au5@Pd2/C) - E(Pd7/C or Au5@Pd2/C) - E(CO) = E$_{ads}$       (1)

for which Pd7/C means seven atoms of Pd on carbon support, Au5@Pd2 means five atoms of Au, and two atoms of Pd. The choice of five atoms of Au and two atoms of Pd holds the proportionality

used in the experimental synthesis of core-shell Au@Pd/C structure. We designed two classes of Au5@Pd2/C, named as [Au5@Pd2/C]A and [Au5@Pd2/C]B.

Designed geometries for the proposed clusters were fully optimized using the B3LYP functional and two basis sets: 6−31++g** for C, H, and O and LANL2DZ for metallic atoms [24]. The same methodology was employed to calculate the adsorption on the clusters, for which only adsorbate was freely optimized. The DFT calculations were performed using Gaussian 09, and the DOS, L-DOS, XPS simulation within Generalized Koopmans' Theorem approach were made using the Multiwfn software [25].

## 3. Results and discussion

### 3.1. DFT calculations and valence band X-ray photoelectron spectroscopy (VB-XPS)

Figs. 1−3 show the structures obtained for Pd7/C and Au5@Pd2/C clusters isolated and with adsorbed CO molecule. Fig. 4 shows the CO normalized and relative adsorption energies for the three systems. The CO adsorption energies on Pd7/C indicate that the adsorption is less favorable when compared with the adsorption on [Au5@Pd2/C]A and [Au5@Pd2/C]B. In the work of Fan et al. [31] they showed that the addition of Ir atoms to Pd atoms favors the CO oxidation, and they also showed that the CO bridge type in Pd cluster is highly favored.
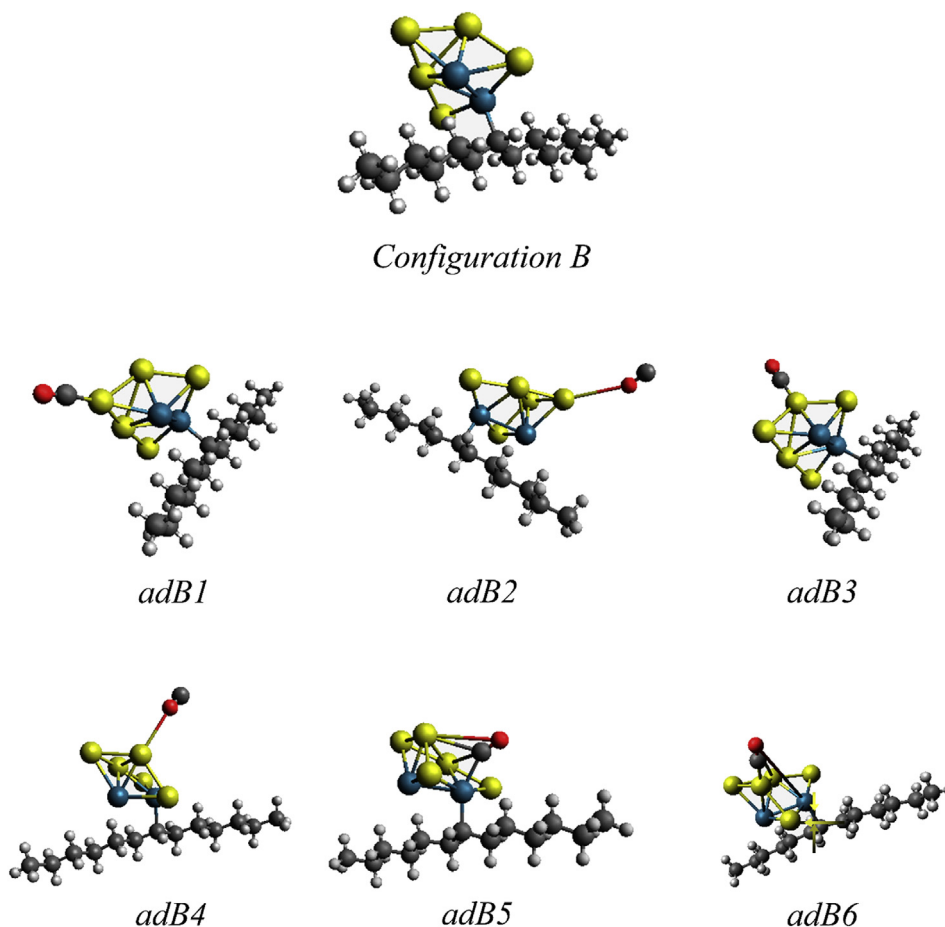


*Configuration B*

*adB1*        *adB2*        *adB3*

*adB4*        *adB5*        *adB6*

**Fig. 2.** Obtained geometry for configuration B [Au5@Pd2/C]B and CO adsorption geometries. Yellow balls are Au atoms, blue ones are Pd atoms, red ones are oxygen atoms, dark gray ones are carbon atoms, and white balls are hydrogen atoms. (For interpretation of the references to color in this figure legend, the reader is referred to the Web version of this article.)
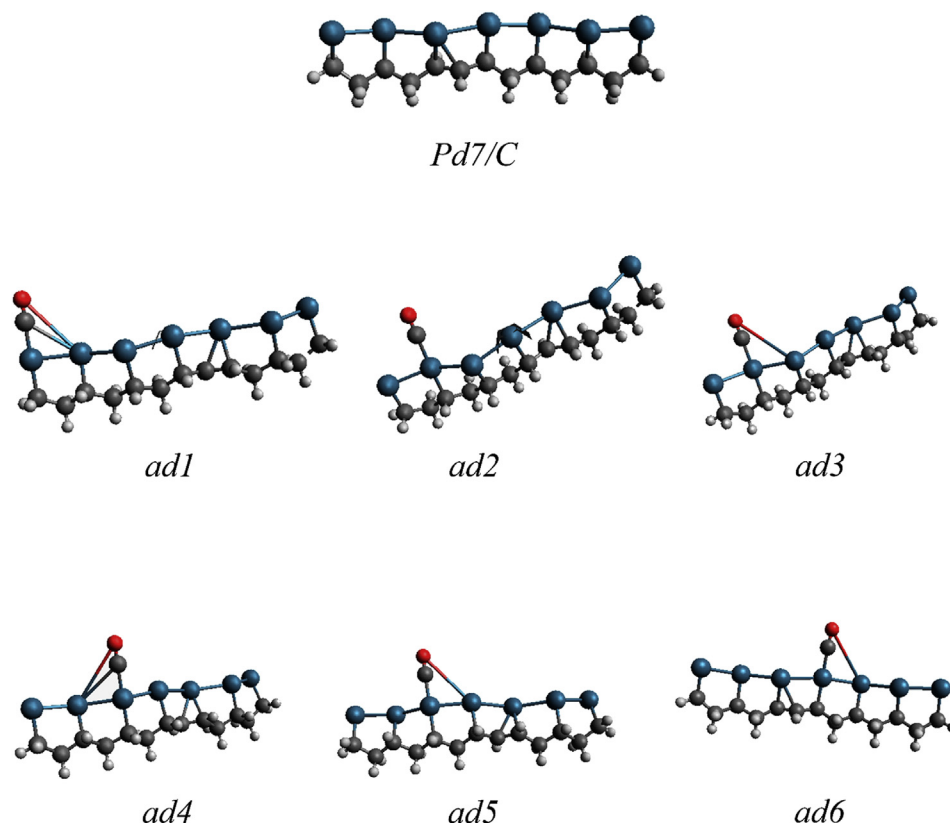
**Fig. 3.** Obtained geometry for Pd7/C and CO adsorption geometries. Blue balls are Pd atoms, red ones are oxygen atoms, dark gray ones are carbon atoms, and white balls are hydrogen atoms. (For interpretation of the references to color in this figure legend, the reader is referred to the Web version of this article.)

There are some adsorption configurations in which oxygen is preferable to be adsorbed in Pd metal active site, which is also observed concerning CO [19] and $CO_2$ [24] adsorption on Pd atoms obtained by DFT calculations, whereas there are other adsorption configurations in which carbon atoms are preferable to be adsorbed on Pd atoms. Furthermore, for [Au5@Pd2/C]A, the adsorption energy increases when the carbon atom of CO binds to Pd atom. This situation is favorable because the Pd atoms are more exposed rather than the Pd atoms in [Au5@Pd2/C]B configuration. We can also notice that the most of the CO adsorption on Au atoms in [Au5@Pd2/C]B is less favorable rather than on [Au5@Pd2/C]A, but the Pd atoms contribute to increase the adsorption energy when it is bonded to the oxygen atom from the CO molecule.

From the thermodynamics point of view, adA4 configuration of [Au5@Pd2/C]A is the most stable configuration among all configurations studied and has the geometric optimization of Au5@Pd2/C + CO similar to what is found in the Nano-EDS one nanoparticle imaging, as we will show in the experimental section.

The increase in the adsorption energy of CO in [Au5@Pd/C]A and [Au5@Pd/C]B is mainly because the presence of Au atoms has increased the Pd-L-DOS below Fermi level as Fig. 7 shows (red line). The virtual orbitals can then be occupied by CO valence electrons; hence, the CO adsorption in [Au5@Pd2/C]A and [Au5@Pd2/C]B induced a decrease in the virtual orbitals and an increase in the occupied orbitals near at Fermi level as Fig. 7 also shows. The Pd-L-DOS, as we referred above, means L-DOS calculated in Pd atoms of the [Au5@Pd2/C]A and [Au5@Pd2/C]B structures and [Au5@Pd2/C]A $_i$, i = 1, 2 or [Au5@Pd2/C]B $_i$, i = 1, 2 means the first and second Pd atom in the structure.

The increase of virtual states in Pd-L-DOS can be explained by the Newns−Anderson−Grimley theory [32−36]. The Hamiltonian
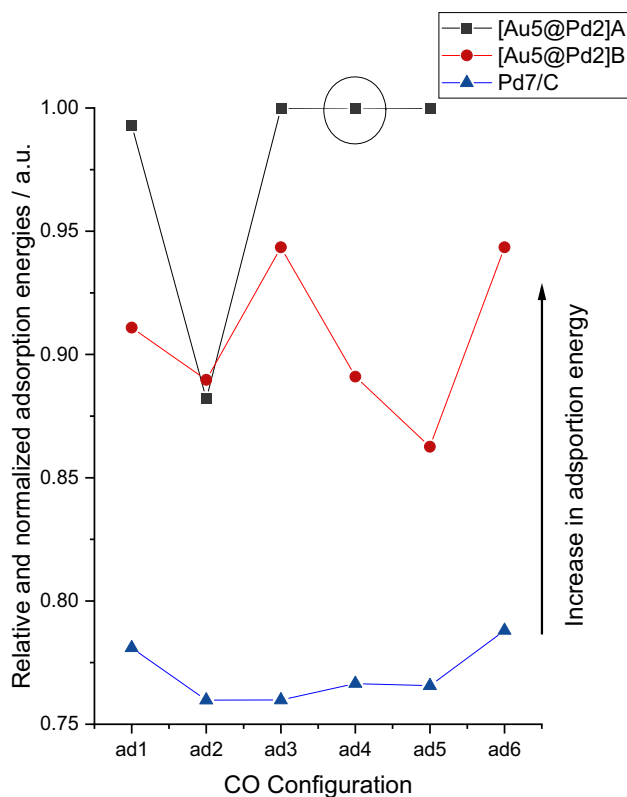


**Fig. 4.** Relative and normalized CO adsorption energy in different active sites on Pd7/C, [Au5@Pd2/C]A and [Au5@Pd2/C]B. The configuration with a circle represents the higher adsorption energy.

that describes the interaction between the Au d-band and the Pd orbital is given by Ref. [36]:

$$H = \sum_{\sigma}\varepsilon_a n_{a\sigma} + \sum_{k,\sigma}\varepsilon_k n_{k,\sigma} + \sum_{k,\sigma}\left(V_{ak}c^{\dagger}_{a\sigma}c_{k\sigma} + H.c.\right) + Un_{a\sigma}Un_{a-\sigma} \quad (2)$$

Using the Green's function associated with the Hamiltonian above we have:

$$G^{\sigma}(\varepsilon) = \left[(\varepsilon + is)I - H\right]^{-1} \quad (3)$$

Equation (3) leads to the following matrix equation, which can be solved in the unperturbed representation:

$$(I\varepsilon - H)G(\varepsilon) = I \quad (4)$$

$$G_{aa}(\varepsilon) = \left[\varepsilon - \varepsilon_{\sigma} - \sum_{k}\frac{|V_{ak}|^2}{\varepsilon - \varepsilon_k + is}\right]^{-1} = \left[\varepsilon - \varepsilon_{\sigma} - \wedge(\varepsilon) + i\Delta(\varepsilon)\right]^{-1} \quad (5)$$

where, specifically for our system: $\Delta(\varepsilon) = \pi\sum_{k}|V_{Au \text{ and } Pd}|^2\delta(\varepsilon - \varepsilon_{Au})$ is the weighted DOS function and $\wedge = H(\Delta(\varepsilon)) = \frac{P_r}{\pi}\int_{-\infty}^{+\infty}\frac{\Delta(\varepsilon')d\varepsilon'}{\varepsilon - \varepsilon'}$ is the Hilbert transform of the weighted DOS function.

Fig. 5 shows the graphical solution obtained to the above model for our system in the strong coupling regime. The green semi-elliptical d band of Au interacts with Pd orbital. This interaction between d-band and adsorbate states is known to be strong (V [2] > W), where V is the interaction strength and W is the d band-width. This situation leads to the formation of bonding and anti-bonding rehybridized states, where its position is determined by the intersection between the Hilbert transform (black dotted line) and the adsorption function (red line). This intersection is represented by the black circles in Fig. 5A.

Furthermore, the d-band center theory has stated that the pseudomorphic layer (Pd shell in Au core atoms) can decrease the d-bandwidth, thus causing a displacement in the d-band center toward Fermi level. These same authors, Gorzkowski and Lewera and Pereira and Miranda [17,19] have shown, using XPS valence band spectra and DFT with van der Waals interaction, that the d-band center moves in the opposite direction of Fermi level.
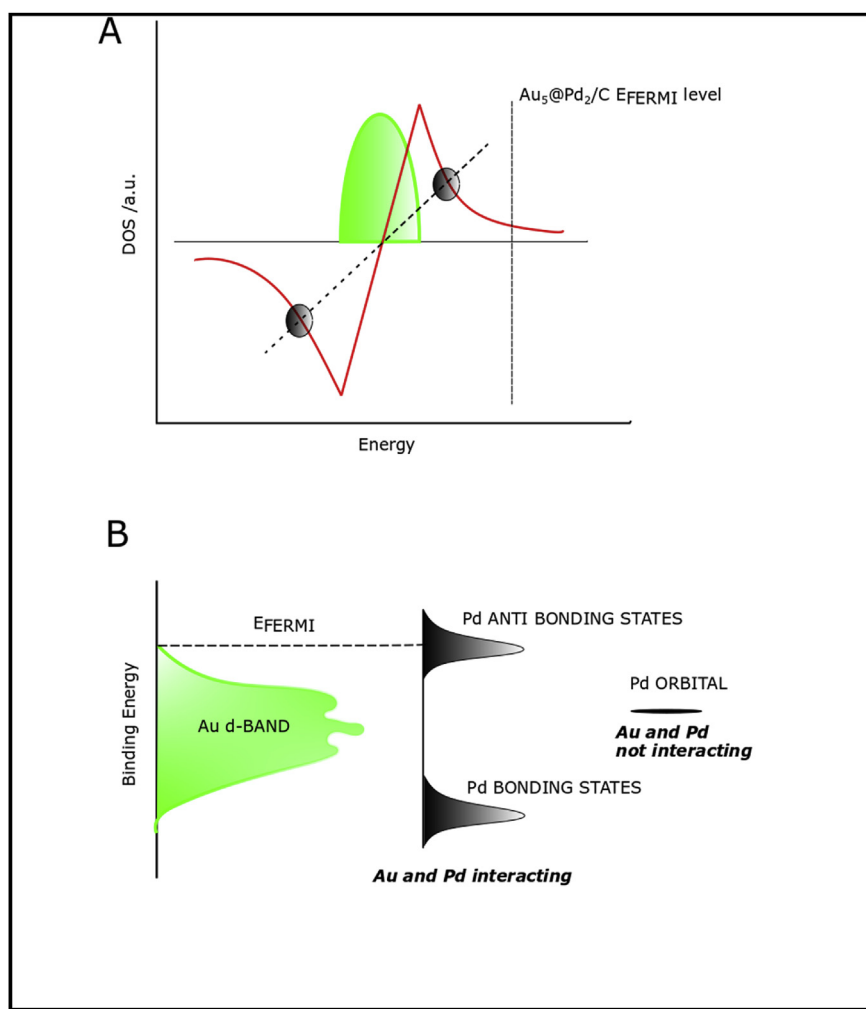


Fig. 5. A. Strong coupling regime between Au d-Band and Pd orbital states. The green semielliptical curve represents the d-band of Au, the red line represents the adsorption function, and the black circles are the bonding and antibonding states. B. Pd orbital splitting because of the interaction between Au d-band and Pd orbital states. (For interpretation of the references to color in this figure legend, the reader is referred to the Web version of this article.)
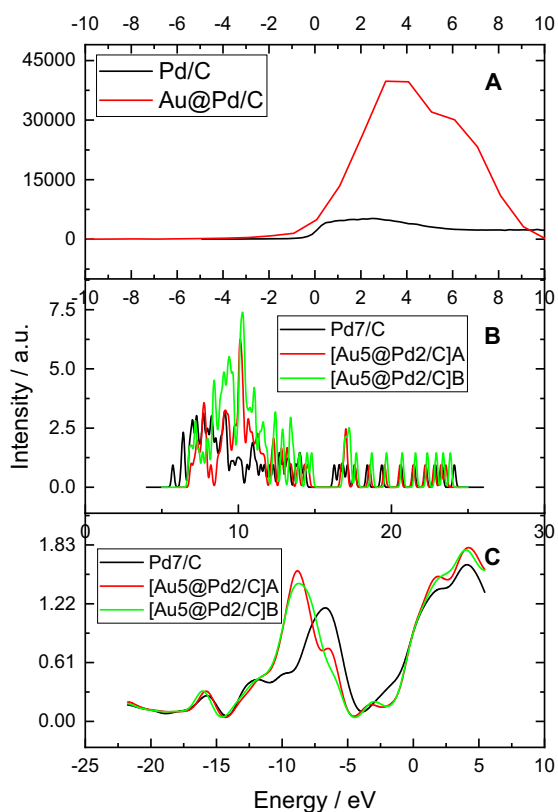
**Fig. 6.** **A.** Experimental VB-XPS for Pd/C and Au@Pd/C. **B.** Simulated XPS using the Generalized Koopman's Theorem for Pd7/C, [Au5@Pd2/C]A and [Au5@Pd2/C]B.**C.** DOS of Pd7/C, [Au5@Pd2/C]A and [Au5@Pd2/C]B.
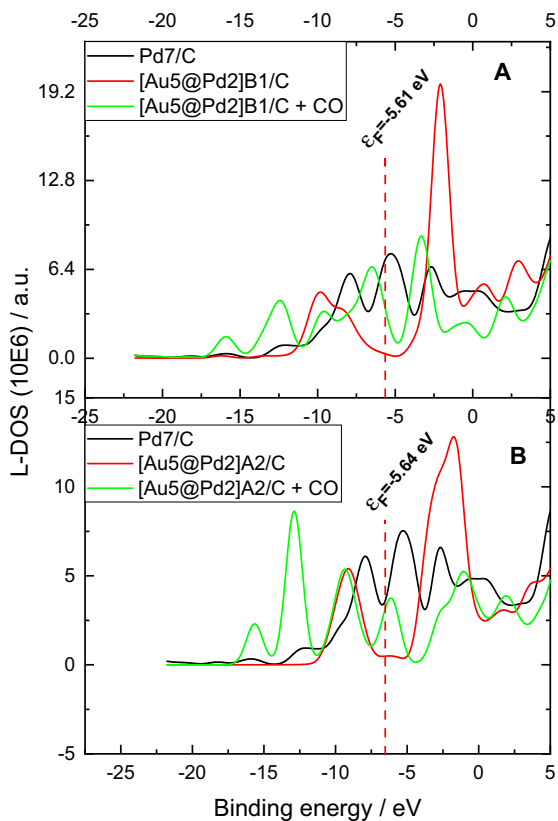


**Fig. 8.** Ethanol products of reaction vs. potential applied in 1 mol L$^{-1}$ KOH +1 mol L$^{-1}$ C$_2$H$_5$OH. The applied potentials were from −0.85V to 0.05V.



**Fig. 7.** **A**. L-DOS of Pd7/C, [Au5@Pd2]B1/C and [Au5@Pd2]B1/C + CO. **B.** L-DOS of Pd7/C, [Au5@Pd2]A2/C and [Au5@Pd2]A2/C + CO. L-DOS, local density of state.
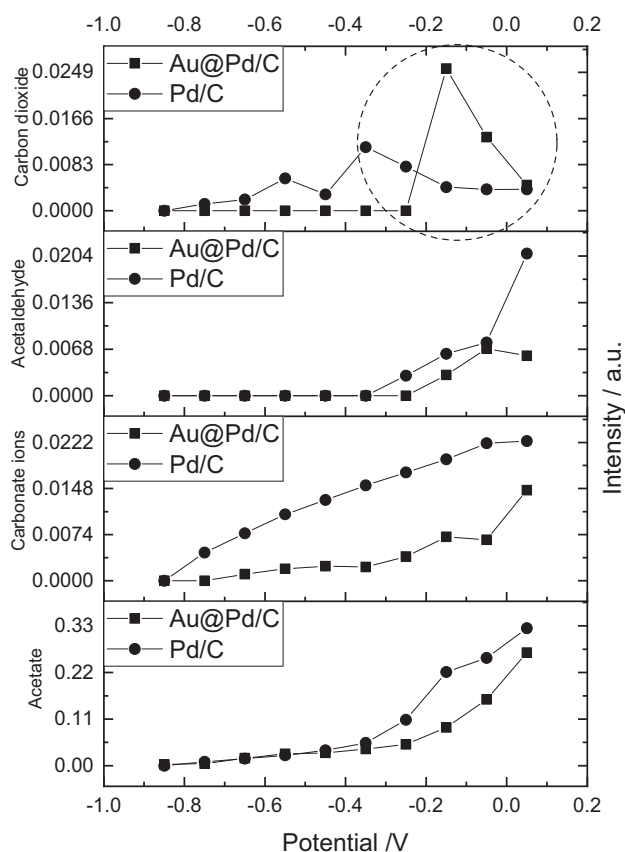
Gorzkowski and Lewera [17] have also shown an increase in d-DOS near Fermi level caused by the Pd monolayer deposited over Pt core nanoparticles. As Fig. 6C shows, the result above mentioned can also explain the stronger adsorption between Pd active sites in Au@Pd/C and CO similarly to what is described in literature [17,19].

Using VB-XPS measurements as shown in Fig. 6A and studying the effect of Au atoms in Pd/C by DFT, we showed that an increase in DOS near Fermi level actually happens, which is also in agreement with study by Gorzkowski and Lewera [17] We also noticed by VB-XPS and DFT that the d-band center shifts away from the Fermi level, which is also in agreement with studies by Gorzkowski and Lewera and Pereira and Miranda [17,19]. But, we are stating here that the increase in DOS near at Fermi level is important for the increase in CO adsorption energy only because the virtual orbital states can be occupied by the valence electrons of CO molecule, as we already discussed.

Using the GKT [37,38], we simulated the VB-XPS for Pd7/C, [Au5@Pd2/C]A and [Au5@Pd2/C]B structures as Fig. 6B shows, and we found that the center of the d-band actually shifts toward away from Fermi level as we also predicted by DOS calculation and experimental VB-XPS. These results are in accordance with study by Gorzkowski and Lewera [17]. It is noteworthy to mention that the valence electrons of Au are indeed a d states which have bonding energy of Au5d in 12.51 eV and Au6s in 6.50 eV [17].

### 3.2. ATR-FTIR spectroscopy

Fig. 8 shows CO$_2$, C$_2$H$_4$O, CH$_3$COO$^-$, and CO$_3^{2-}$ band intensity. Although the electrolyte is an alkaline type, the interface between
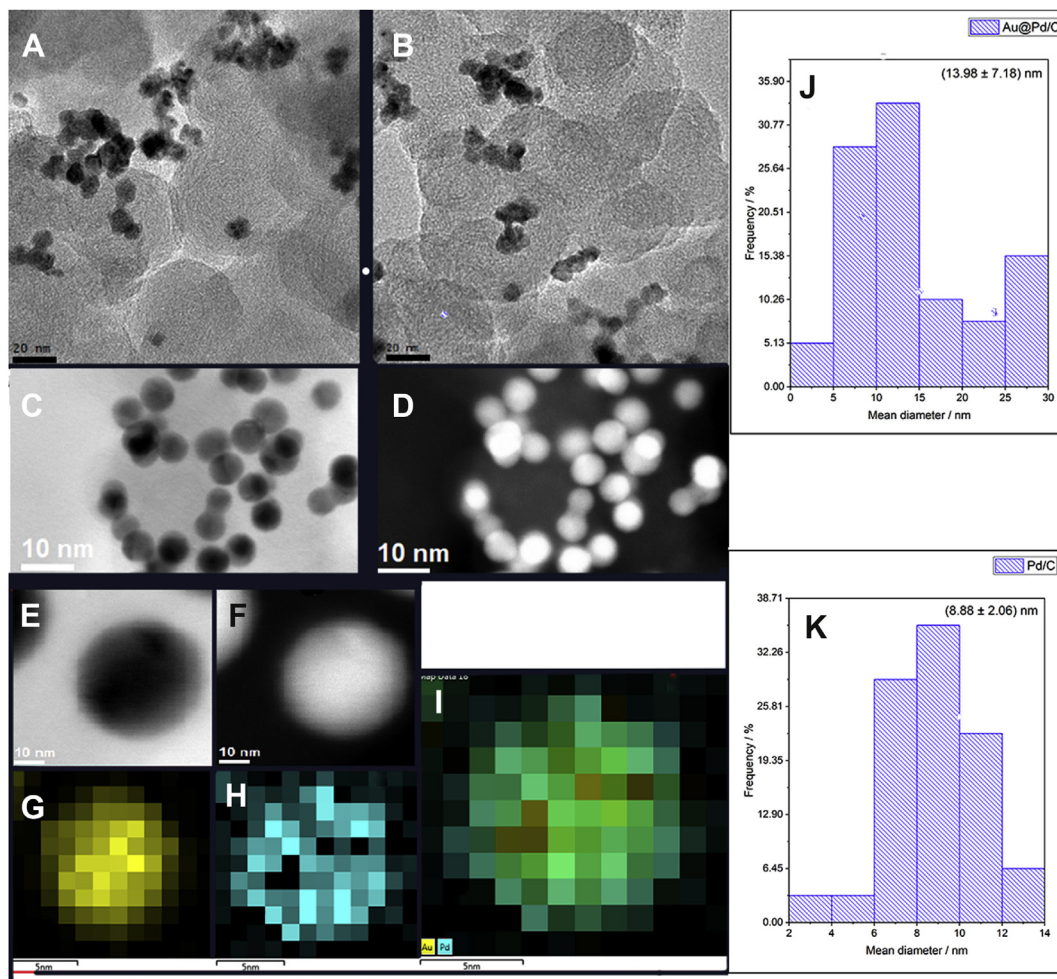
**Fig. 9. A-B).** TEM images of Pd/C. (**C−F**). STEM images of Au@Pd/C. (**G**). Au Nano-EDS. (**H**). Pd Nano-EDS. (**I**). Au@Pd/C Nano-EDS. (**J-K**). Nanoparticles mean diameter of Pd/C and Au@Pd/C.

the electrode and the electrolyte can turn to be an acidic type [39], so $CO_2$ and aldehyde species can be stable in this region.

It was possible to observe ethanol products of reaction as a function of the potential applied. It was found that for Au@Pd/C, the $CO_2$ increases in the high potential applied regime (~-0.15 V). Besides that, $C_2H_4O$ production tends to increase for all potentials applied (except at the last potential probed 0.05 V). Still for Au@Pd/C, $CO_3^{2-}$ production has the highest increase initiated at −0.05 V, which coincides with the $CO_2$ decrease (in some extension, the $CO_2$ molecule is interacting with the KOH medium forming $CO_3^{2-}$).

All these results combined with the fact that $CH_3COO^-$ is an ethanol product of the reaction and not an ethanol intermediate of reaction and using the mechanism of reaction proposed in study by Kamarudin et al. [13], we strongly suggest that $CO_2$ production is via CO or $CH_x$ oxidation. We showed through DFT calculations that $CO_{ads}$ is more stable in Au5@Pd2/C rather in Pd/C. Thus, the $CO_2$ production could be obtained through CO oxidation reaction.

The intermediate $CO_{ads}$ could not be identified in this ATR-FTIR setup because the electrode is placed in a certain distance from the ATR crystal. It is important to point out here that the carbonate ions production for Pd/C is almost a straight line, so we cannot ensure that this process is due to the C−C ethanol bond cleavage or it is a simple ambient contaminant.

### 3.3. STEM and Nano-EDS

The nanoparticle's shape and distribution of Pd/C and Au@Pd/C were characterized by transmission electron microscopy (TEM), scanning transmission electron microscopy (STEM), and Nano-energy dispersive spectroscopy (EDS) techniques. As we can see in Fig. 9A−B, the Pd nanoparticles were anchored in the Carbon Vulcan XC72 structure, but the shape distribution is not homogenous because some agglomerates can be observed. However, the Au@Pd nanoparticles presented a very spherical symmetry shape. The key factor for this kind of spherical nanoparticle shape is the use of oleylamine as reducing and capping agent [27,40]. The nanoparticle's mean diameter obtained by the use of oleylamine for the synthesis of Au@Pd/C is very similar to what is reported in the literature [27,40], and the same goes for Pd/C using sodium borohydride [29]. The analysis of the Au@Pd/C and Pd/C images were fundamental to design the structures used in the DFT analysis, as we briefly discussed in the materials and methods section.

### 3.4. Electrochemical results

Fig. 10A shows the chronoamperometry for Pd/C and Au@Pd/C in alkaline medium. At approximately 1740 s, the performance of Au@Pd/C surpasses Pd/C. This can be explained by two factors: first, core-shell nanoparticles have higher stability than other types of
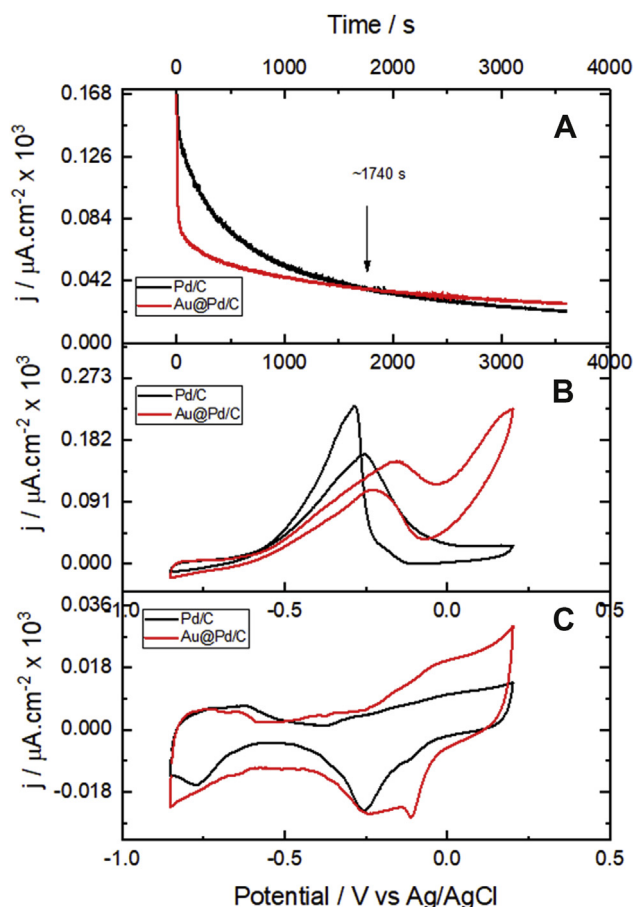
**Fig. 10. A**. Chronoamperometry of Pd/C and Au@Pd/C at −0.35 V in 75 mmol L$^{-1}$ of C$_2$H$_5$OH and 0.5 mol L$^{-1}$ of KOH. **B**. Cyclic voltammetry of Pd/C and Au@Pd/C also in 75 mmol L$^{-1}$ of C$_2$H$_5$OH and 0.5 mol L$^{-1}$ of KOH. **C**. Cyclic voltammetry of Pd/C and Au@Pd/C in 0.5 mol L$^{-1}$ of KOH The curves were normalized by electrochemical surface area (ECSA) and the anodic scan was set to 10 mV s$^{-1}$.

nanoparticles [11,41]. Second, at −0.35 V, the CO$_2$ production starts for Au@Pd/C granting higher current densities, as we can see in Fig. 7. Because the acetate production is higher for Pd/C at −0.35 V as well as for the carbonate ions, probably, Pd atoms are not so good to avoid these kinds of poisonings effects.

Fig. 10B shows the CV for Pd/C and Au@Pd/C in 0.5 mol L$^{-1}$ KOH and 75 mmol L$^{-1}$ C$_2$H$_5$OH. The fuel concentration for this work is following the study by Li et al. [11]. The onset potential is higher for Pd/C than for Au@Pd/C. This can be explained by the fact that the ethanol molecules start its oxidation in higher potentials for Au@Pd/C. But, we can also notice that for potentials above −0.25 V, Au@Pd/C has higher current densities, which agrees with the CO$_2$ production for this same material.

Fig. 10C shows the CV for Pd/C and Au@Pd/C only in 0.5 mol L$^{-1}$ KOH. The hydrogen adsorption/desorption process [42] is well defined for Au@Pd/C, indicating that the Pd atoms are indeed in the shell of the structure Au@Pd/C. The double-layer region is higher for Au@Pd/C than for Pd/C, as well as the two peaks associated with the PdO$_x$ formation in the range of −0.25 V and 0.1 V [42]. The two peaks in the reverse scan are associated with the reduction of the oxide species. It is noteworthy to mention that these species can oxidize the CO$_{ads}$/(CH$_x$)$_{ads}$ to CO$_2$, because the PdO$_x$ and OH$^-$ species are in the vicinity of the intermediate adsorbed species [19,22,42].

## 4. Conclusion

Au@Pd/C showed an excellent performance to produce CO$_2$ and has a better electrochemical activity when compared with Pd/C. Through DFT calculations, we showed that the CO oxidation pathway is energetically favorable in Au@Pd/C, when it is also compared to Pd/C. The increase in CO adsorption energy in Au@Pd/C can be explained by the fact that Au5 induces an increase in virtual orbitals states in Pd2, as we have verified by Pd-L-DOS. Also, the Newns−Anderson−Grimley model can explain this increase.

The higher stability of Au@Pd/C, as well as the ability to produce CO$_2$, is evident in the chronoamperometry experiments when compared with Pd/C. At approximately 1740s, the performance of Au@Pd/C surpasses Pd/C. In the CV experiments, the current density observed for Au@Pd/C is higher, which is also because of the formation of CO$_2$ species. It is noteworthy to mention that the interface of the electrode and the electrolyte suffers acidification, making it possible to aldehyde and CO$_2$ species to be stable.

ATR-FTIR spectroscopy was capable to identify the presence of CO$_2$, CO$_3^{2-}$, C$_2$H$_4$O, C$_2$H$_5$OH, and CH$_3$COO$^-$ species, but it was not possible to observe the presence of possible intermediates, such like CO and CH$_x$ species.

## Credit author statement

**Eric H Fontes:** Conceptualization, Data curation, Writing-Original draft preparation. **Paula H de Mello, Felipe Antonio:** Software, Editing, Reviewing: **Almir Oliveira Neto:** Supervision. **Julio Nandenha e Rodrigo de Souza:** Reviewing.

## Declaration of competing interest

The authors declare that they have no known competing financial interests or personal relationships that could have appeared to influence the work reported in this paper.

## Acknowledgments

## References

[1] S. Zhang, et al., Chin. J. Catal. 40 (12) (2019) 1904.
[2] K.S. Ju, et al., Chem. Phys. Lett. 727 (2019) 78.
[3] L.S.R. Silva, et al., Appl. Catal. B Environ. 251 (2019) 313.
[4] X.-J. Zhang, et al., Molecular Catalysis 436 (2017) 138.
[5] J. Wang, et al., Int. J. Hydrogen Energy 44 (31) (2019) 16411.
[6] J. Wang, et al., Appl. Catal. B Environ. 259 (2019) 118060.
[7] H.Ö. Doğan, Solid State Sci. 98 (2019) 106029.
[8] Z. Zhang, et al., Int. J. Hydrogen Energy 44 (13) (2019) 6608.
[9] C.S. Sharma, et al., Int. J. Hydrogen Energy 38 (35) (2013) 15388.
[10] I. Velázquez-Hernández, et al., Fuel (2019) 116556.
[11] C. Li, et al., Sensor. Actuator. B Chem 171−172 (2012) 1192.
[12] X. Qiu, et al., J. Power Sources 278 (2015) 430.
[13] M.Z.F. Kamarudin, et al., Int. J. Hydrogen Energy 38 (22) (2013) 9438.
[14] F. Mollarasouli, et al., Int. J. Hydrogen Energy 44 (39) (2019) 22085.
[15] R. Ojani, et al., Electrochim. Acta 56 (9) (2011) 3380.
[16] Y. Kwon, et al., J. Am. Chem. Soc. 133 (18) (2011) 6914.
[17] M.T. Gorzkowski, A. Lewera, J. Phys. Chem. C 119 (32) (2015) 18389.
[18] C. Hsu, et al., Electrochem. Commun. 23 (2012) 133.
[19] A.O. Pereira, C.R. Miranda, Appl. Surf. Sci. 288 (2014) 564.
[20] B. Hammer, et al., Phys. Rev. Lett. 76 (12) (1996) 2141.
[21] B. Hammer, Top. Catal. 37 (1) (2006) 3.
[22] B. Miao, et al., Comput. Mater. Sci. 156 (2019) 175.
[23] T.F.M. de Souza, et al., Dyes Pigments 172 (2020) 107824.
[24] A.G. Saputro, et al., J. Phys. Conf. 739 (2016) 012083.

[25] T. Lu, F. Chen, J. Comput. Chem. 33 (5) (2012) 580.

[26] G.S. Buzzo, et al., J. Power Sources 199 (2012) 75.

[27] D. Chen, et al., Sci. Rep. 5 (2015) 11949.

[28] E.H. Fontes, et al., Mater. Renew. Sustain. Energy 4 (1) (2015) 3.

[29] E.H. Fontes, et al., Int. J. Hydrogen Energy 44 (2) (2019) 937.

[30] H. Xiao-Zi Yuan, W. Jiujun Zhang, PEM Fuel Cell Electrocatalysts and Catalyst Layers Fundamentals and Applications, Springer-Verlag London Springer, 2008.

[31] T.-E. Fan, et al., Phys. Chem. Chem. Phys. 19 (39) (2017) 27090.

[32] D.M. Newns, Phys. Rev. 178 (3) (1969) 1123.

[33] P.W. Anderson, Phys. Rev. 124 (1) (1961) 41.

[34] M.T. Greiner, et al., Nat. Chem. 10 (10) (2018) 1008.

[35] S.Z. Vlaev, Surf. Sci. 274 (1) (1992) 185.

[36] R. Taranko, et al., Surf. Sci. 231 (1−2) (1990) 113.

[37] D. Kröner, et al., Surf. Sci. 605 (15) (2011) 1516.

[38] B. Yang, et al., J. Phys. Chem. 122 (51) (2018) 9886.

[39] M.C. Figueiredo, et al., Chem. Electro. Chem 2 (9) (2015) 1254.

[40] M.V. Kirichkov, et al., Radiat. Phys. Chem. (2018), https://doi.org/10.1016/j.radphyschem.2018.11.021.

[41] Q. Tan, et al., J. Catal. 295 (2012) 217.

[42] F. Zhang, et al., J. Energy Chem 25 (1) (2016) 71.

[43] E. Franco-Junior, et al., J. Power Sources 273 (2015) 360.